Heterometallic perovskite-type metal-organic framework with an ammonium cation: structure, phonons, and optical response of $[NH_4]Na_{0.5}Cr_xAl_{0.5-x}(HCOO)_3$ (x=0, 0.025 and 1)

Maciej Ptak,*[,a] Dagmara Stefańska,[a] Anna Gągor,[a] Katrine L. Svane,[b,c] Aron Walsh,[d,e] and Waldeci Paraguassu[f]

[a]*Institute of Low Temperature and Structure Research, Polish Academy of Sciences, Wrocław, Poland*

[b]*Department of Chemistry, University of Bath, Bath, United Kingdom*

[c]*Department of Energy Conversion and Storage, Technical University of Denmark, Lyngby, Denmark*

[d]*Department of Materials, Imperial College London, London, United Kingdom*

[d]*Department of Materials Science and Engineering, Yonsei University, Seoul, Korea*

[f]*Faculty of Physics, Federal University of Para, Belém, Brazil*

ABSTRACT

We report the synthesis, crystal structure, vibrational and luminescence properties of two heterometallic perovskite-type metal-organic frameworks (MOFs) containing the ammonium cation (NH_4^+, Am^+): $[NH_4][Na_{0.5}Cr_{0.5}(HCOO)_3]$ (AmNaCr) and $[NH_4][Na_{0.5}Al_{0.475}Cr_{0.025}(HCOO)_3]$ (AmNaAlCr) in comparison to the previously reported $[NH_4][Na_{0.5}Al_{0.5}(HCOO)_3]$ (AmNaAl). The room-temperature crystal structure of AmNaCr and AmNaAlCr was determined to be $R\overline{3}$. The hydrogen bonding (HB) energy calculated using density functional theory (DFT) agrees well with experimental data, and confirms the existence of almost identical H-bonding in AmNaCr and AmNaAl, with three short hydrogen bonds and a longer trifurcated H-bond. Temperature-dependent Raman measurements supported by differential scanning calorimetry show that AmNaCr does not undergo any structural phase transitions in the 80–400 K temperature range. The high-pressure Raman spectra of AmNaCr show the onset of two structural instabilities near 0.5 and 1.5 GPa. The first instability involves weak distortion of the framework, while the second leads to irreversible amorphization of the sample. High-pressure DFT simulations show that the unit cell of the AmNaCr compound contracts along the *c* axis, which leads to a shortening of the trifurcated H-bond. The optical

properties show that both studied crystals exhibit Cr^{3+}-based emission characteristic of intermediate ligand field strength.

1. Introduction

It is well known that inorganic perovskites with the general formula ABX_3 exhibit interesting physical phenomena, such as colossal magnetoresistance or ferroelectricity.[1,2] Hybrid organic-inorganic perovskites consist of a metal-anionic framework with cavities large enough to accommodate positively charged organic cations, typically protonated amines, on the A-site. These compounds have attracted a lot of attention in recent years due to their multifunctionality and easy methods of synthesis from solution. The sub-group containing halide atoms on the X site have been recognized as very attractive materials for thin-film photovoltaic devices,[3–6] while the sub-group with formate anions on the X site have been extensively studied due to their magnetic, ferroelectric, multiferroic and luminescent properties.[7,8,17–19,9–16]

The formate perovskites studied so far have primarily been based on divalent metal ions on the B site. Recently, however, the synthesis of heterometallic MOFs has become possible and the presence of different metal centers has expanded the range of potential applications. Yu *et al*. have reported the synthesis of a series of bimetallic formate perovskites with the general formula $[AH][Na_{0.5}Al_{0.5}(HCOO)_3]$, where AH denotes NH_4^+, $NH_2NH_3^+$, $CH_3NH_3^+$, $C_2H_2NH_3^+$, $C_2H_5NH_3^+$, $NH_2(CH_3)_2^+$, $NH_3(CH_2)_2NH_3^{2+}$, $CH_3NH_2(CH_2)_2NH_3^{2+}$ $NH_3(CH_2)_3NH_3^{2+}$, $CH_3NH_2(CH_2)_2NH_2CH_3^{2+}$, $NH_3(CH_2)_2NH_2(CH_2)_2NH_3^{3+}$ and $NH_3(CH_2)_2NH_2(CH_2)_2NH_2(CH_2)_2NH_3^{4+}$ cations.[20] Our previous studies have been focused on the bimetallic formate perovskites with the dimethylammonium ($(CH_3)_2NH_2^+$, DMA^+) and ethylammonium ($C_2H_5NH_3^+$, EtA^+) cations with the aim to identify the structural features that are responsible for the occurrence or absence of structural phase transitions in $[cat][M^I_{0.5}M^{III}_{0.5}(HCOO)_3]$ (cat=DMA^+, EtA^+, $M^I = Na^+$, K^+ and $M^{III}=Cr^{3+}$, Al^{3+} and Fe^{3+}).[19,21–24] We have shown that the HB arrangement and type of $M^IO_6/M^{III}O_6$ structural units are crucial factors determining the flexibility of the framework and thereby the susceptibility to symmetry change.[23] We have also shown that the heterometallic formate frameworks containing Cr^{3+} ions exhibit efficient emission in spite of concentration quenching, therefore such compounds are good candidates for optical applications.[21,23,24]

Herein, we report the synthesis and properties of two heterometallic formate frameworks templated with Am^+ cations, i.e., $[NH_4][Na_{0.5}Cr_{0.5}(HCOO)_3]$ (AmNaCr) and $[NH_4][Na_{0.5}Al_{0.475}Cr_{0.025}(HCOO)_3]$ (AmNaAlCr). We have chosen the Am^+ cations because former studies of formate based frameworks with divalent metal ions showed that employment of these small cations can significantly alter structural and electric properties of the material. For instance, ammonium metal formates crystallize in chiral-type structures and exhibit second-order ferroelectric phase transitions, whereas analogues with much larger cations, such as DMA^+, crystallize in perovskite-type architectures and exhibit first-order phase transitions.[19,23] The synthesized structures are studied by X-Ray diffraction and found to be isostructural with the previously reported $[NH_4][Na_{0.5}Al_{0.5}(HCOO)_3]$ (AmNaAl) structure, crystallizing at room temperature in the trigonal $R\bar{3}$ spacegroup.[20] The materials are further investigated by Differential Scanning Calorimetry (DSC), Infra-Red (IR) and Raman spectroscopy in order to better understand the correlation between structural parameters and the presence/absence of a structural phase transition. We also report high-pressure Raman scattering studies. To date, only a few papers report the high-pressure behavior of perovskite-type formate MOFs, and these have solely been composed of divalent metal ions, such as Mg^{2+}, Mn^{2+} and Zn^{2+}.[25–29] Among them one concerns the chiral-type $[NH_4][Zn(HCOO)_3]$ and its deuterated analogue $[ND_4][Zn(HCOO)_3]$, which undergo a structural phase transition at about 1.1 GPa associated with strong deformation of the formate framework.[26] Finally, we investigate the effect of the stronger crystal field on the luminescence and optical properties of these materials when Cr^{3+} ions are replaced by smaller Al^{3+} ones.

The experimental studies are supported by density functional theory (DFT) calculations to verify the determined structural features and assist in the assignment of strongly coupled lattice vibrations. Furthermore, we calculate the hydrogen bonding energy and simulate high-pressure conditions in order to understand the changes related to HB during the experiment. Our results reveal that the materials do not undergo any temperature-induced phase transition due to the strong HBs, but that the HBs are affected by an increased pressure, resulting in a phase transition at a pressure of 0.5 GPa.

2. Experimental

2.1. Materials and instrumentation

All reagents (analytically grade) used for synthesis were commercially available and were used without further purification. The powder XRD (X-Ray Diffraction) patterns were obtained on an X'Pert PRO X-ray

diffraction system equipped with a PIXcel ultrafast line detector, focusing mirror, and Soller slits for Cu Kα radiation (λ=1.54056 Å). The DSC measurement of AmNaCr was performed in the temperature range 140–400 K on a DSC-7 instrument (Perkin-Elmer) at a rate of 5˚C/min under a nitrogen atmosphere (Fig. S1). The fresh crystalline powdered sample of AmNaCr (6.63 mg) was used. Room-temperature Raman spectra were collected using a Bruker FT 110/S spectrometer with 2 cm^{-1} resolution. The temperature-dependent Raman spectra were measured in a Linkam THMS600 cryostat cell using a Renishaw InVia Raman microscope equipped with confocal DM 2500 Leica optical microscope, a thermoelectrically cooled CCD as a detector and an argon laser operating at 488 nm. IR (Infrared) spectra in the mid-IR (4000–400 cm^{-1}) and far-IR (400–50 cm^{-1}) range were measured in KBr pellets and nujol suspension on the polyethylene plate, respectively, using a Nicolet iS50 FT-IR (Fourier Transform Infrared) spectrometer with 2 cm^{-1} resolution. The high-pressure Raman spectra were recorded in back-scattering geometry using a microscope attached to a triple-grating spectrometer Jobin Yvon T64000. The 514.5 nm line of a solid-state ion laser was used as excitation and the spectral resolution was 2 cm^{-1}. In order to reach high pressures, a diamond anvil cell Diacell® μScopeDAC-RT(G) from Almax easyLab with a diamond of 0.4 mm of culets was used. The sample was loaded into a 100 mm hole drilled in a stainless steel gasket with a thickness of 200 mm using an electric discharge machine from Almax easyLab. The Nujol served as the pressure transmitting media. Pressures were measured based on the shifts of the ruby R_1 and R_2 fluorescence lines. For luminescence measurements at 300 K and 77 K, the Hamamatsu photonic multichannel analyzer PMA-12 equipped with a BT-CCD linear image sensor and Nd:YAG laser as the excitation source were used. A temperature of 77 K was obtained using liquid nitrogen and a Dewar flask. For measurements at 10 K, the Jobin-Yvon measurement system, along with a helium close cycle cryostat, was used. Decay profiles were recorded with a Lecroy digital oscilloscope with the Nd:YAG laser as the excitation source. The reflectance absorption spectra were measured with the Varian Cary 5E UV-VIS-NIR spectrophotometer.

2.2. Synthesis of the samples

In order to obtain AmNaCr crystals 1 mmol (0.2664 g) of $CrCl_3 \cdot 6H_2O$ was dissolved in 15 ml of CH_3OH (solution A) and a mixture of 6 mmol (0.4081 g) of HCOONa, 6 mmol (0.3784 g) of $HCOONH_4$ and 5 ml of 98 wt. % of HCOOH was dissolved in 15 ml of CH_3OH (solution B). The solution B was transferred to a glass tube and the less dense solution A was slowly dropped to obtain a liquid-liquid interface between two solutions. The glass tube

was sealed and left undisturbed.[30] The violet crystals of AmNaCr, grown on the surface of the tube, were harvested after one week, washed three times with methanol and dried at 50 ˚C in air. The light pink crystals of AmNaAlCr were prepared in the same way using a mixture of 0.95 mmol (0.3564 g) of $Al(NO_3)_3 \cdot 6H_2O$ and 0.05 mmol (0.0133 g) of $CrCl_3 \cdot 6H_2O$. The phase purity of both bulk samples were confirmed by the good match of their powder XRD patterns with a simulation from the single-crystal structural data (Fig. S2) performed by us for AmNaCr (see the further sections of this paper).

2.3. Crystallographic structure determination

Single-crystal X-ray diffraction data were collected on the Xcalibur Atlas diffractometer equipped with a Mo*K*α radiation source and a CCD camera. Intensities were measured in ω-scan mode with Δω=1.0 ˚. CrysAlis PRO[31] was used for collection and reduction of the data. Empirical absorption correction with spherical harmonics was done using the multi-scan approach implemented in SCALE3 ABSPACK.[31] The structure was solved in SHELXS and refined in SHELXL2014/7.[32] Hydrogen atoms were included in geometric positions (C–H~0.96 Å, N–H~0.89 Å) and treated as riding atoms. The $U_{iso}(H)$ values were constrained to be $1.2U_{eq}$ (carrier atom).

2.4. Quantum chemical calculations

DFT calculations were performed using the Vienna *ab initio* simulation package (VASP)[33] with PAW pseudopotentials. We used the PBEsol exchange-correlation functional[34] with the D3 correction[35,36] to account for dispersive interactions. The positions and unit cell dimensions are relaxed until all forces are below 0.01 eV/Å using an energy cutoff of 700 eV. Calculations are performed for the newly synthesized AmNaCr compound as well as previously synthesized AmNaAl.[20] The structure of AmNaAlCr is computationally unfeasible to model, as the low concentration of Cr ions requires a large unit cell, but it is expected to closely resemble that of AmNaAl. We use a 2×2×1 k-point mesh for the unit cells which contain 6 ammonium cations. For the structure containing Cr^{3+}, the calculations are spin-polarised. Initial calculations for EtAKCr (to be published) showed an energy difference of less than 1 meV between the ferromagnetic and antiferromagnetic ordering of the magnetic moments on the Cr^{3+} ions, and the correct magnetic ordering is thus beyond our computational accuracy. We have chosen to optimise the structure with ferromagnetic alignment of the spins on the Cr^{3+} ions. Harmonic phonon calculations are performed for AmNaCr using the finite displacement method as implemented in VASP. We use the 1×1×1 primitive unit cell

(containing two organic cations) and therefore only frequencies at the gamma point are considered. Phonopy[37] is used to calculate the vibrational frequencies and assign symmetries to the individual modes.

The hydrogen bonding energy for AmNaCr and AmNaAl is calculated following the procedure in Ref. 37.[38] The dominating monopole part of the electrostatic interaction is subtracted from the total electrostatic interactions, and the remaining dipole and higher order terms are assumed to be dominated by the hydrogen bonding. The total electrostatic interaction is calculated as the energy required to remove one A-site cation from the unit cell, while the monopole term is estimated as the energy required to remove a single cation from the same cage. In the original publication[38] a Cs^+ was used as the cation, however, since the cage volumes of AmNaCr and AmNaAl are quite small (187 and 186 $Å^3$/cation, respectively) we also calculate the H-bonding energy using K^+ as a reference.

3. Results and discussion

3.1. Crystal structure

The crystal structure of AmNaCr is isomorphic with the previously reported structures of DMANaFe, DMANaCr[19,24] and AmNaAl[20] and is shown in Fig. 1a. The lattice constants are given in Table 1, while full experimental details can be found in Tab. S1. The inorganic part adopts a perovskite-like architecture as shown in Fig. 1b. It consists of CrO_6 and NaO_6 octahedra, which are linked by the formate units in *anti-anti* connection mode (Fig. 1 and S3). Each sodium ion has six chromium atoms as nearest metal neighbours and *vice versa*. This results in asymmetric C–O bond lengths in the formate groups of 1.255(3) for the C–$O1_{Cr}$ bond and 1.216(3) Å for the C–$O2_{Na}$ bond. The most important bond lengths are given in Tab. 1, while a more detailed list of bond lengths and angles are given in Tab. S2.

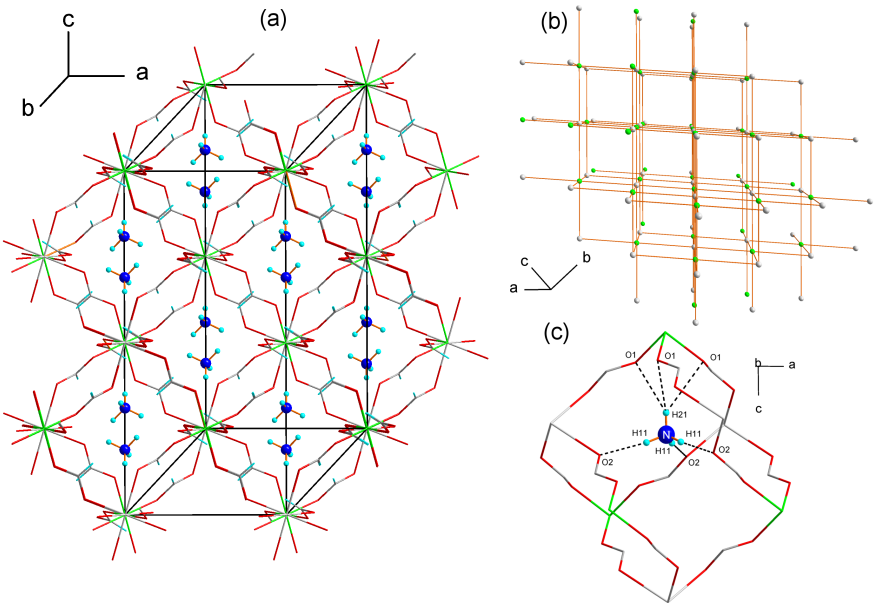

Fig. 1. (a) Packing of the crystal structure of AmNaCr, (b) perovskite-like topology of the inorganic network and (c) N–H···O HBs between the NH_4^+ template and the formate ligands.

The NH_4^+ cations are located in large cavities and interact with the inorganic part *via* N–H···O HBs. The symmetry of the NH_4^+ cations is compatible with the site symmetry of the nitrogen position (C_3) thus the molecule is ordered and forms three relatively short N2–H···O2 HBs and one longer, trifurcated N2–H···O1^{i} interaction with the metal-formate framework. The N–O distances are 2.852 and 3.324 Å for AmNaCr and 2.837 and 3.286 Å for AmNaAlCr,[20] the more detailed geometry is given in Tab. S3. Fig. 1c shows the position of the NH_4^+ cation in a cavity and the HBs. Due to the small size of the cation and the symmetry matching between NH_4^+ and its site symmetry, the volume of the unit cell (V=1173.1(2) Å^3) is much smaller than for the disordered DMANaCr analogue (V=1382.2(4) Å^3) where the DMA^+ cations may adopt three different placements in one perovskite cavity. This small size of the Am^+ cation results in geometric tolerance factors of 0.65–0.66, much lower than the values that would typically be expected for a perovskite structure (0.7–1.0).[39]

3.2. DFT structure optimisation

The DFT optimised unit cell parameters of the AmNaCr and AmNaAl compounds are compared with the experimental values in Tab. 1. In general the optimised volumes are slightly smaller than the experimental values as have also previously been observed for the chosen functional,[38] and this leads to slightly shorter HB lengths,

however the general agreement is good. These differences are consistent with the absence of temperature (lattice thermal expansion) in the DFT simulations. The three short HBs between the NH_4^+ cations and the formate groups of the cage are found to relax to H–O distances of 1.71 Å (1.71 Å) for the AmNaCr (AmNaAl) compounds, while the last hydrogen of NH_4^+ points directly towards the Cr^{3+} ion with equal distances to the three nearest oxygens of 2.45 Å (2.44 Å). The corresponding N–O distances are given in Table 1 for comparison with the experimental values. The similar bond lengths in the two compounds suggest that the HBs have similar strength. Our calculations also confirm the experimentally observed asymmetry of the formate anions, where the C–O2–Na^+ bond is slightly shorter (1.252 Å and 1.251 Å for AmNaCr and AmNaAl, c.f. Table 1) than the C–O1–$(Cr/Al)^{3+}$ bond (1.286 Å and 1.283 Å for AmNaCr and AmNaAl, c.f. Table 1). A difference in bond length is not surprising given the difference in charge and electronegativity of the cations. Na has a lower electronegativity than Cr and Al (0.9 vs. 1.7/1.6) and thus forms a more ionic bond with oxygen.

	AmNaCr		AmNaAl	
	Exp. (298 K)	DFT calc.	Exp. (293 K)[20]	DFT calc.
Space group	$R\bar{3}$	$R\bar{3}$	$R\bar{3}$	$R\bar{3}$
a=*b* (Å)	7.939	7.83	7.903	7.81
c (Å)	21.494	21.12	21.359	21.08
V (Å^3)	1173.1	1122.3	1155.4	1113.1
γ (°)	120	120	120	120
N2–O2 (Å)	2.852	2.77	2.837	2.76
N2–O1 (Å)	3.324	3.30	3.286	3.30
C–O1 (Å)	1.255(3)	1.286		1.283
C–O2 (Å)	1.216(3)	1.252		1.251

Tab. 1. Experimental and (DFT/PBEsol+D3) calculated unit cell parameters for AmNaCr and AmNaAl, along with selected bond lengths.

3.3. Raman and IR studies – selection rules, phonon calculations and assignment of modes

The vibrational spectra of the studied crystals may be understood by dividing the Brillouin zone-centre (q=0) vibrations into internal vibrations of the organic and formate ions, and the lattice vibrations. The free formate ion has C_{2v} symmetry and has six fundamental vibrations ($3A_1+3B_1$): stretching CH vibration (ν_1), the symmetric stretching CO mode (ν_2), the antisymmetric stretching CO mode (ν_4), the symmetric OCO bending (scissoring) mode (ν_3), the CH in plane bending mode (ν_5) and the CH out of plane bending mode (ν_6).[40] AmNaCr crystallizes in the trigonal structure, space group $R\overline{3}$, with six (two) formulas per unit (primitive) cell. Therefore, the number of internal modes of the $HCOO^-$ ions increases to 36 ($6A_g+6A_u+6E_g+6E_u$), as presented in Tab. S4. The free Am^+ (NH_4^+) cation has T_d symmetry and 4 internal vibrations (A_1+E+2F_2): $\nu_1(A_1)$ symmetric stretching, $\nu_2(E)$ symmetric bending, $\nu_3(F_2)$ antisymmetric stretching and $\nu_4(F_2)$ antisymmetric bending.[41] According to the factor group analysis (see Tab. S4), the number of internal modes related to the Am^+ cation increases to 18 ($3A_g+3A_u+3E_g+3E_u$). Our analysis also show that AmNaCr crystal should show the presence of $3A_g+3A_u+3E_g+3E_u$, $3A_g+3A_u+3E_g+3E_u$, $A_g+A_u+E_g+E_u$, $A_g+A_u+E_g+E_u$, A_u+E_u and A_u+E_u lattice modes corresponding to translations (T') of $HCOO^-$, librations (L) of $HCOO^-$, translations of Am^+, librations of Am^+, translations of Cr^{3+}, and translations of Na^+ ions, respectively. Therefore, the expected total number of modes is 108 ($17A_g+19A_u+17E_g+19E_u$), including 105 optical ($17A_g+18A_u+17E_g+18E_u$) and 3 acoustic ones (A_u+E_u). All g-symmetry modes of AmNaCr are Raman-active, wherein only the u-symmetry modes are IR-active. Thus the total number of expected Raman and IR bands is 34 ($17A_g+17E_g$) and 36 ($18A_u+18E_u$), respectively.

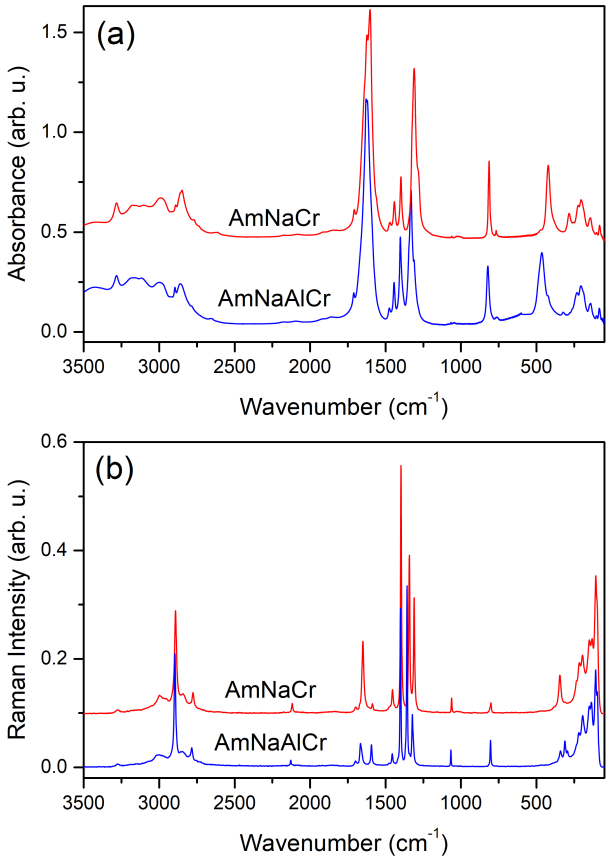

Fig. 2. Room temperature IR (a) and Raman (b) spectra of polycrystalline AmNaCr (red lines) and AmNaAlCr (blue lines).

Fig. 2 presents Raman and IR spectra of AmNaCr and AmNaAlCr measured at ambient conditions. The observed Raman and IR band positions as well as proposed assignments of all vibrational modes are listed in Tab. S5. The strong and characteristic bands corresponding to formate ions are located in very narrow ranges, therefore, their assignment can be easily obtained based on the rich literature data for various MOFs containing formate ions.[16,17,27–29,40,42,18,19,21–26] That is, the internal modes of the $HCOO^-$ ions are observed at 2858–2893 (ν_1), 1587–1652 (ν_4), 1344–1399 (ν_5), 1285–1326 (ν_2), 1068 (ν_6) and 768–815 cm^{-1} (ν_3) for AmNaCr and at 2861–2897 (ν_1), 1594–1668 (ν_4), 1359–1403 (ν_5), 1311–1346 (ν_2), 1068 (ν_6) and 763–823 cm^{-1} (ν_3) for AmNaAlCr.

The assignment of bands corresponding to the internal vibrations of the NH_4^+ ions can be obtained based on the DFT-based lattice dynamics performed for $[NH_4][Zn(HCOO)_3]$.[26] According to this paper, the $\nu_1(NH_4^+)$ symmetric and $\nu_3(NH_4^+)$ asymmetric stretching vibrations are expected in the 3142–3556 cm^{-1} range and at about 2877 cm^{-1}, respectively, while $\nu_2(NH_4^+)$ symmetric and $\nu_4(NH_4^+)$ antisymmetric bending vibrations are predicted at

about 1730–1740 and 1465–1537 cm^{-1}, respectively.[42] Our IR spectra show presence of many broad bands above 2850 cm^{-1} that were assigned to ν_1 and ν_3 vibrations. Remaining bending vibrations were found at 1701–1709 cm^{-1} (1701–1712 cm^{-1}) and 1443–1485 cm^{-1} (1445–1478 cm^{-1}) for AmNaCr (AmNaAlCr).

It is well known that if a bond participates in formation of HBs, its stretching vibration shifts to lower wavenumbers while the bandwidth increases. Tab. S5 shows that stretching modes of the NH_4^+ ions are observed at very similar wavenumbers for AmNaAlCr and AmNaCr, implying similar strength of HBs in both compounds. This behaviour is consistent with X-ray diffraction data and DFT calculations, which show similar N–H···O_{Na} and N–H···O_{Al} bonds for both compounds (c.f Table 1). Significant upshifts, reaching up to 21, 15 and 26 cm^{-1} for the $\nu_1(NH_4^+)$, $\nu_5(NH_4^+)$ and $\nu_2(NH_4^+)$ modes, respectively, are however observed when going from AmNaCr to AmNaAlCr. This behaviour can most likely be attributed to the significantly smaller mass and effective radius of the Al^{3+} ions. The smaller size of Al^{3+} compared to Cr^{3+} also leads to a larger distortion of the metal-formate framework of AmNaAlCr.

In the low wavenumber region, below 500 cm^{-1}, the IR and Raman spectra show some differences which are expected due to the differences in mass and size of the trivalent ions. It is well known that the wavenumber of a translational mode should be approximately proportional to the square root of the reciprocal reduced mass.[42] In our case, the factor group analysis (see Tab. S4) shows that bands corresponding to translations of Cr^{3+}/Al^{3+} as well as Na^+ ions have A_u and E_u symmetry, therefore they are exclusively IR-active and should be absent in Raman spectra. Indeed, for AmNaCr we observe strong IR bands at 284 and 424 cm^{-1} that are strongly up-shifted to 323 and 465 cm^{-1} for AmNaAlCr. These bands can be attributed to translational modes of Cr^{3+} and Al^{3+} ions, respectively. Based on our previous studies of heterometallic MOFs,[19,21–24] we assign the IR bands located at 226 (232) and 258 cm^{-1} to transational modes of Na^+ in AmNaCr (AmNaAlCr).

The assignment of translations and librations of formate ions and Am^+ cations is more complicated due to their coupling. However, according to literature data, T'(NH_4^+) and L(NH_4^+) are usually observed in the 160–270 and 300–480 cm^{-1} range, respectively.[42–44] The DFT calculations made for [NH_4][Zn($HCOO)_3$] showed that they are expected in the 107–215 and 248–613 cm^{-1} range, respectively.[26] As one can notice, L(NH_4^+) modes are expected to coincide with T'(M^{3+}) ones, however, their positions should be less sensitive to a change of trivalent ions. We assign, therefore, the Raman band at 345 (342) cm^{-1} and the IR band at 475 (483) cm^{-1} to librations of the NH_4^+ ions. Literature data shows that the intensity of T'(NH_4^+) modes is stronger in IR spectra and weaker in Raman spectra

whereas the opposite behavior is observed for T'($HCOO^-$) modes.[27,42] Thus, we assign the strongest Raman bands in the 132–221 cm^{-1} range to translations of the formate ions and some weak IR bands in the 144–312 cm^{-1} range to vibrations with the strongest contribution coming from Am^+ translational motions. Remaining bands, below 113 cm^{-1}, can be assigned to librations of the formate ions.[19,21–24]

To confirm the correctness of the proposed assignments we have performed harmonic phonon calculations. Tab. S5 contains only the assignments of the strongest contribution of each mode but Tab. S6 lists experimental values along with assignments based on the calculated displacement vectors contributing for every vibration. Close inspection of the obtained data shows a good match between calculated and experimental wavenumbers corresponding to the lattice modes. In the internal modes region the divergence becomes higher since the applied model excludes anharmonic (phonon-phonon) interactions. Our previous DFT calculations of hydrazine and its single protonated cation revealed the strongly anharmonic nature of the stretching $\nu(NH_2)$ and/or $\nu(NH_3^+)$ modes.[45] They also showed that the wavenumbers calculated in the anharmonic approximation gave much lower values for many vibrational modes.

3.4. Temperature-dependent Raman studies

The temperature-dependent Raman spectra of AmNaCr are presented in Fig. 3, whereas Fig. 4 presents the temperature-dependent evolution of wavenumbers and full width at half maximum (FWHM) for selected bands. The Raman spectra and temperature evolution of wavenumbers and FWHM show no anomalies that could indicate presence of a structural phase transition. This behaviour is consistent with structural and DSC data. It is worth noting, however, that at room temperature some bands are very broad and may overlap with other bands, causing weak and broad bands to appear invisible. Thus, the appearance of new bands at lower temperatures results only from the narrowing of very broad bands and associated increase in intensity. It is worth adding that the number of observed Raman bands at 80 K (35) is in a very good agreement with the predicted one by group theory (34). This is a further proof that the observed thermal evolution of the spectra is not related to any phase transition. Nevertheless, closer inspection of Figs. 3 and 4 shows some interesting features. Firstly, the intense and relatively narrow band assigned to $\nu_1(NH_4^+)$ located at 2846 cm^{-1} becomes very broad with increasing temperature. This is a typical feature observed for MOFs that exhibit order-disorder phase transition due to ordering of templated amines.[19,21–24] Due to the absence of a structural phase transition in the studied crystal and also in pure AmNaAl,[20] the observed behaviour

is attributed to increased thermal motion of the NH_4^+ ions and associated anharmonic. Secondly, the majority of the modes show usual hardening upon cooling, without any significant departure from the expected behaviour due to temperature-dependent anharmonic decays (see Figs. 4 and S4 in which expected phonon behaviour obtained using the methodology described in details earlier,[46] is presented as solid lines). The $\nu_4(HCOO^-)$ and $\nu_2(HCOO^-)$, however, show hardening down to about 200–225 K, followed by softening below this temperature (see Figs. 4c, 4e and S4c). Former X-ray diffraction studies of AmNaAl showed that the crystallographic C–O bond lengths of the $HCOO^-$ ions increase upon cooling, i.e., $C–O_{Al}$ ($C–O_{Na}$) increase from 1.2591 Å (1.2247 Å) at 293 K to 1.2743 Å (1.2346 Å) at 100 K. Since the $\nu_4(HCOO^-)$ and $\nu_2(HCOO^-)$ modes involve stretching vibrations of the C–O bonds, we suppose that their peculiar behaviour can be attributed to contributions of two factors, i.e., hardening related to phonon anharmonic decay and softening related to increase of C–O bond lengths upon cooling. In the temperature range down to 200–225 K, the first contribution prevails over the second one and we observed hardening of these modes but below 200–225 K the second contribution becomes dominant, leading to the observed softening.

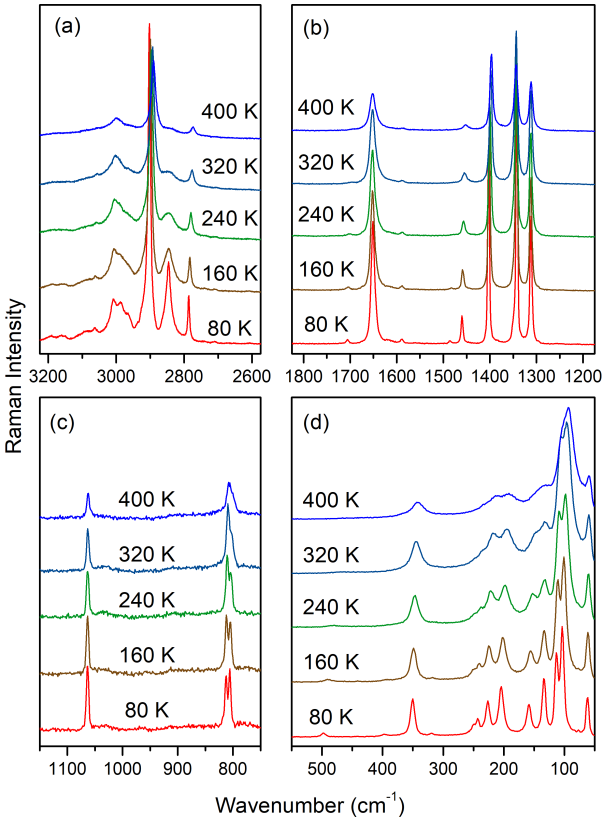

Fig. 3. The temperature-dependent Raman spectra in (a) 3225–2575, (b) 1825–1175, (c) 1150–750 and (d) 550–50 cm^{-1} ranges at selected temperatures.

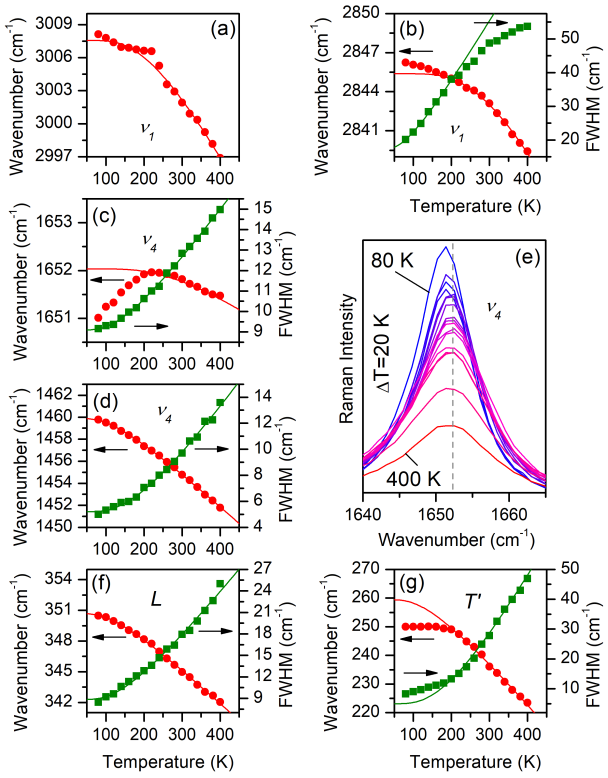

Fig. 4. Temperature evolution of wavenumber (red circles, left scales) and FWHM (green squares, right scales) for selected Raman bands corresponding to (a, b) $\nu_1(NH_4^+)$ (symmetric stretching), (c, e) $\nu_4(HCOO^-)$ (antisymmetric stretching), (d) $\nu_4(NH_4^+)$ (antisymmetric bending), (f) NH_4^+ librational and (g) NH_4^+ translational modes.

3.5. Phase transitions, hydrogen bonding and structural flexibility

It is interesting to try to understand the lack of structural phase transitions for AmNaAl and AmNaCr, in contrast to $[NH_4][Zn(HCOO)_3]$.[26] Several important factors have been highlighted in previous publications, including the strength of the HBs, the difference in vibrational entropy between phases and the ability of the framework to deform.[19,21–24,38,47,48]

For $[NH_4][Zn(HCOO)_3]$ there is only one type of octahedral building blocks, while in the case of heterometallic compounds with two different metal ions, leading to octahedral units that have different size and flexibility. The bonds created between Na^+ and oxygen ions have more ionic character than those formed by oxygen

and Cr^{3+}/Al^{3+} ions, and because of this the alternately located NaO_6 and $Cr(Al)O_6$ octahedra can significantly change the size of the voids that accommodate the ammonium ions. This can suppress the occurrence of an order-disorder phase transition, as we previously showed for the heterometallic MOFs with ethylammonium and dimethylammonium cations.[19,21–24]

The strength of the HB is calculated for the two Am^+ compounds, following the procedure described in ref 37.[38] The results are given in Tab. 3, along with the volume per cation (V_{cation}), the tolerance factors (*TF*), and the range of values previously calculated for $[A]Zn(HCOO)_3$ perovskites (A=guanidinium, hydrazinium, azetidinium or dimethylammonium cation).[38]

	AmNaCr	AmNaAl	$[A]Zn(HCOO)_3$[38]
Cs^+ ref.			
E_{tot} (eV)	1.80	1.81	0.36–1.40
$E_{N–H}$ (eV)	0.45	0.45	0.18–0.28
K^+ ref.			
E_{tot} (eV)	0.82	0.86	0.07–1.12
$E_{N–H}$ (eV)	0.21	0.22	0.04–0.19
V_{cation} (Å^3)	187	186	186–213
TF	0.65	0.66	0.81–0.96

Tab. 3. Total hydrogen bonding energies (E_{tot}) and HB per N–H bond in the cation ($E_{tot}/n_{N–H}$) for the two NH_4^+ heterometallic perovskites calculated using both Cs^+ and K^+ as a reference, along with the range of values previously calculated for Zn^{2+} based formate perovskites. We also give the volume per cation (V_{cation}) and the tolerance factor (*TF*), calculated as described previously.[47]

We use the same computational setup as previously,[38] such that the results should be directly comparable. However, using Cs^+ as a reference, the calculated HB energy per N–H bond in the cation, which was found to be

similar for all the Zn^{2+} formate perovskite[38] (see Tab. 3), is very high. This could be a result of steric interactions when the NH_4^+ cation is replaced with a Cs^+ cation, since the cage volume is relatively small and the effective radius of Cs^+ (165 pm) is larger than that of NH_4^+ (146 pm).[47] Therefore we also performed calculations with the smaller K^+ cation (radius of 133 pm), however we still find that the HB energy is high for the NH_4^+ compounds compared with the previously calculated Zn based compounds. This could be a result of the mixed metal composition, which leads to a more ionic O-Na^+ bond (compared with O-Zn), and thereby to a larger fractional charge δ^- on the oxygen atom. The strong HB energy is consistent with the absence of phase transitions below the decomposition temperature of ca. 420 K.

3.6. Pressure-dependent Raman spectra

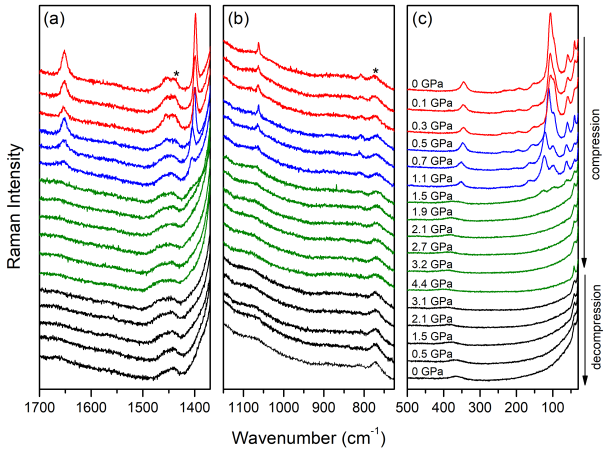

Fig. 5. The pressure-dependent Raman spectra of AmNaCr during compression and decompression experiments. The stars denote the signal of the pressure-medium.

To better understand the physicochemical properties of the studied MOFs we submitted AmNaCr to high pressure conditions. Fig. 5 shows Raman spectra measured up to 4.4 GPa in the selected regions and Fig. 6 shows the pressure evolution for the observed modes. The spectrum measured at ambient conditions is nearly the same as that obtained outside the pressure chamber. The signal is slightly weaker and some additional bands corresponding to the pressure medium (nujol) are observed at 775 and 1438 cm^{-1}. The pressure-dependent behavior of all observed modes is well described using a linear function $\omega(P)=\omega_0+\alpha P$ with two factors: ω_0 describing interception at zero pressure and the so-called vibrational pressure coefficient $\alpha=d\omega/dP$ describing the rate of wavenumbers' change to

the pressure unit. The results of fitting and the obtained parameters are summarized in Tab. 2. Fig. 5 and 6 show that the spectra remain almost the same up to a pressure of 0.3 GPa. All modes exhibit an increase in wavenumber in this pressure range (Fig. 6 and Tab. 2). Especially pronounced hardening (11.34 cm^{-1} GPa^{-1}) is observed for the T'(NH_4^+) mode near 190 cm^{-1}. Remaining α parameters corresponding to NH_4^+ ions are also large suggesting that the ammonium ions are strongly affected by the applied pressure. The highest pressure coefficients for vibrations assigned to formate ions are obtained for some of the lattice modes. Those corresponding to C–H stretching and bending vibrations are smaller indicating that under pressure the C–H bonds are less affected than the C–O bonds. We also conclude that metal-oxygen bonds forming octahedral units shorten with increasing pressure.

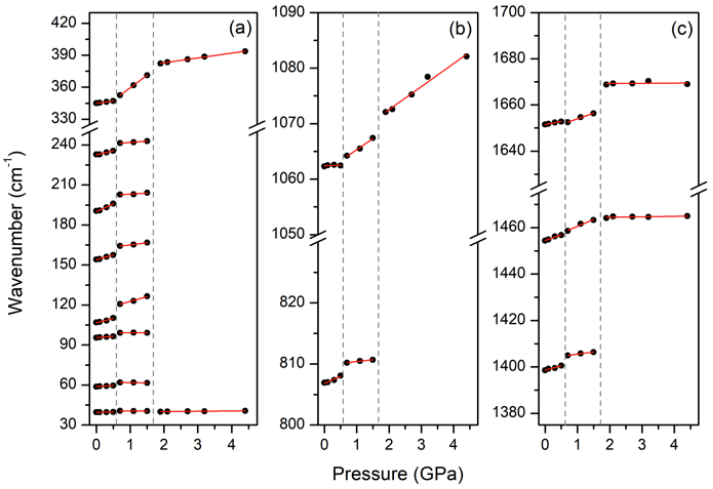

Fig. 6. The pressure-evolution of Raman bands for AmNaCr in (a) 30–430, (b) 800–1090 and (c) 1375–1700 cm^{-1} ranges.

Tab. 2. Raman zero wavenumbers (ω_0) for the three phases of AmNaCr, pressure coefficients (α) obtained from the linear fits on the data together with proposed assignment.

Mode No	Ambient-pressure phase (AP)		High-pressure phase I (HP1)		High-pressure phase II (HP2)		Assignment
	ω_0 (cm^{-1})	$d\omega/dP$ (cm^{-1} GPa^{-1})	ω_0 (cm^{-1})	$d\omega/dP$ (cm^{-1} GPa^{-1})	ω_0 (cm^{-1})	$d\omega/dP$ (cm^{-1} GPa^{-1})	

1	1651.5	2.58	1649.2	4.84	1669.1	0.09	$\nu_4(HCOO^-)$
2	1454.5	5.02	1454.7	5.85	1454.0	0.21	$\nu_4(NH_4^+)$
3	1398.6	3.71	1403.7	1.85			$\nu_5(HCOO^-)$
4	1062.4	0.27	1061.3	3.97	1064.2	4.15	$\nu_6(HCOO^-)$
5	806.8	2.33	809.8	0.59	373.8	4.55	$\nu_3(HCOO^-)$
6	345.0	4.26	335.9	23.6			$L(NH_4^+)$
7	232.7	5.74	240.0	1.91			$T'(NH_4^+)$
8	190.1	11.34	201.6	1.55			$T'(NH_4^+)$
9	154.0	6.82	162.0	3.11	39.6	0.24	$T'(HCOO^-)$
10	106.6	6.72	115.6	7.12			$L(HCOO^-)$
11	95.5	1.96	99.1	0.05			$L(HCOO^-)$
12	58.8	1.54	62.2	-0.43			$L(HCOO^-)$
13	39.5	0.35	40.6	-0.16			$L(HCOO^-)$

A further increase in pressure up to 0.5 GPa leads to a discontinuity in the observed wavenumber shifts and changes in the slope (α) of the wavenumber vs. pressure function. This behaviour indicates that AmNaCr undergoes a pressure-induced phase transition at about 0.5 GPa. However, the total number of observed modes remains the same, suggesting that the trigonal symmetry might be preserved in the HP1 phase. Closer inspection of the high-pressure data shows that the most characteristic change at 0.5 GPa is the strong decrease in intensity of many bands and/or increase in FWHM. In HPI phase the majority of α parameters corresponding to lattice modes decrease, except for modes No 6 and 10 corresponding to librations of Am^+ and formate ions, respectively. Interestingly, the value of α for mode No 6 reaches a very high value equal to 23.6 cm^{-1} GPa^{-1} indicating that increase of pressure in HPI phase strongly affects the Am^+ ions and their HBs with the metal-formate framework. It is also worth noticing that the two lowest wavenumber $L(HCOO^-)$ modes have negative pressure coefficients. Pronounced softening of modes under pressure reveals that anharmonicity becomes important, and it is an indication of some crystal instability.[26,49] In this case libration of the formate unit at fixed volume leads to an increase in the average M–O bond length, and thus becomes more favourable at high pressure where this bond is slightly compressed. The existence of a phase transition is further confirmed by the behavior of the FWHM of the lowest wavenumber Raman

band, i.e., the increase of pressure from 0 to 0.3 GPa leads to strong broadening of this band but it becomes narrow again at 0.5 GPa suggesting that the metal-formate framework is well defined.

When the pressure reaches 1.5 GPa, the Raman spectrum changes drastically. In particular, the intensity of the majority of bands decreases and many of them vanish. As a result, only four Raman bands are observed at 1.5 GPa. The observed changes in the Raman spectra indicate that AmNaCr experiences a second phase transition between 1.1 and 1.5 GPa. The weak intensity of the observed bands and their large widths strongly suggests that AmNaCr starts to amorphize above 1.5 GPa. The decompression experiment shows that the initial phase is not recovered, supporting our conclusion on a pressure-induced amorphization of AmNaCr above 1.5 GPa.

It is worth mentioning that $[ND_4][Zn(HCOO)_3]$ experienced only one phase transition between 0.94 and 1.35 GPa, which was better visible due to the splitting of bands corresponding to formate ions and stretching vibrations of deutered Am^+ ions that were downshifted due to the isotopic effect, which allowed avoiding coincidence with bands of the pressure medium.[26] This sample was compressed up to 5.31 GPa and some features suggested pressure-induced amorphization, however, the initial phase was recovered after decompression.[26] The lowering of the phase transition pressure for AmNaCr and its low pressure of amorphization indicate that this compound is less resistant to the high pressure conditions than $[ND_4][Zn(HCOO)_3]$.

3.7. DFT simulation of high pressure

To gain further insight into the effect of an applied pressure on the structure of AmNaCr we optimised the structure at a fixed volume of 1100 $Å^3$ corresponding to 98% of the optimised volume. The calculated cell stress suggests that this corresponds to an external pressure of 0.44 GPa. The relative length of the unit cell vectors were allowed to change, resulting in a larger relative contraction of the *c* vector (1.4 %) than for the *a* and *b* vectors (0.24 %). The three long HBs are shortened slightly from an H-O distance of 2.45 Å (c.f Table 1) to 2.41, while the three short HBs remain at almost the same length shrinking from 1.71 to 1.70 Å. The larger compression along the *c*-axis is consistent with the experimentally observed hardening of the T'(NH_4^+) mode, which is related to translation along this direction (see ESI for a gif of this mode). The result thus supports our analysis based on the pressure-dependent Raman spectra showing that the ammonium ions are strongly affected by the applied pressure in the ambient pressure (below 0.3 GPa) and HPI (above 0.5 GPa) phases.

3.8. Optical response

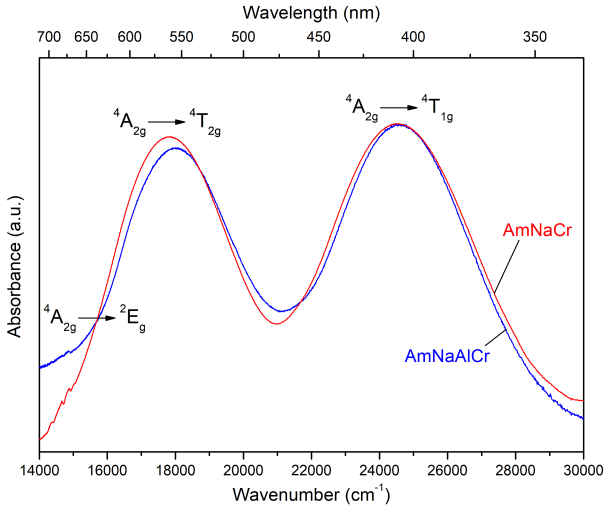

Fig. 7. The diffuse reflectance spectra of AmNaCr and AmNaAlCr measured at 300 K.

The diffuse reflectance absorption spectra of AmNaCr and AmNaAlCr are shown in Fig. 7. The two broad bands characteristic for Cr^{3+} ions at the intermediate ligand field centered at about 18 000 (556 nm) and 24 500 (408 nm) cm^{-1} are observed. The first one is assigned to the spin allowed transition from the ground $^4A_{2g}$ level to the $^4T_{2g}$ excited state, while the higher energy band corresponds to the $^4A_{2g} \rightarrow {}^4T_{1g}$ (F) transition. The spin forbidden transition from the ground state to the $^2T_{1g}$ and ^2E_g levels is visible as small humps at about 14 676 and 14 874 cm^{-1} for AmNaCr and AmNaAlCr, respectively. The exact position of the ^2E_g emitting level was determined from the emission spectra measured at 10 K (see Fig. 8). Crystal field (Dq) and Racah (B) parameters were calculated for the investigated compounds from the diffuse reflectance absorption spectrum. The value of the B parameter was found by setting the determinant (where T_F is energy of the $^4T_1$(F) band) defined below equal to 0.

$$\begin{vmatrix} 10Dq + 12B - T_F & 6B \\ 6B & 10Dq + 3B - T_F \end{vmatrix}.$$

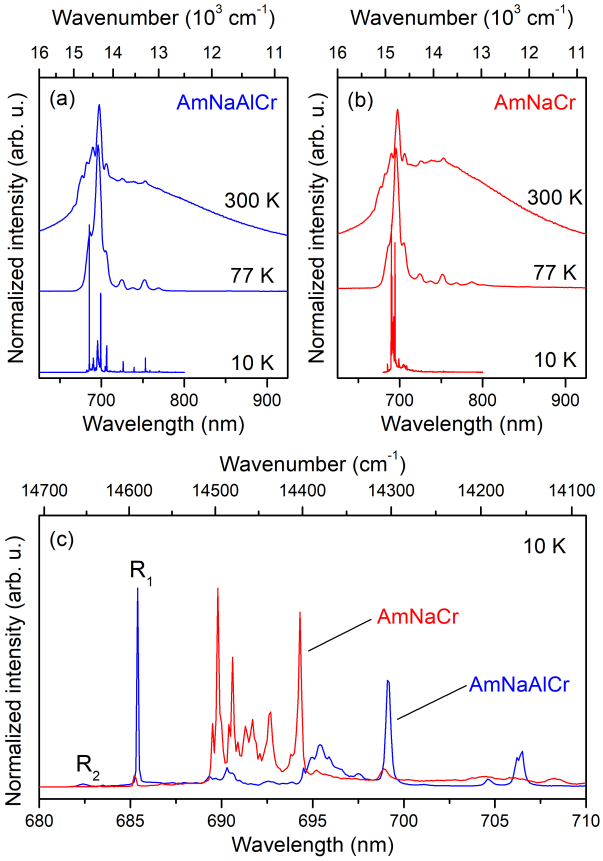

Fig. 8. The emission spectra measured at 300, 77 and 10 K for (a) AmNaAlCr and (b) AmNaCr under 400 nm excitation line. The spectra measured at 10 K were enlarged for comparison (c).

Tab. 2. The crystal field (Dq) and Racah (B) parameters for AmNaCr and AmNaAlCr crystals.

Compound	Dq (cm^{-1})	B (cm^{-1})	Dq/B
AmNaCr	1782	733	2.43
AmNaAlCr	1801	706	2.55

The calculated values are presented in Tab. 2. The Dq/B parameters are equal to 2.43 and 2.55 for AmNaCr and AmNaAlCr, respectively. In the Tanabe-Sugano diagram, the ^2E_g and $^4T_{2g}$ levels overlap for Dq/B=2.3. This point separates the so-called weak (Dq/B < 2.3) and strong (Dq/B > 2.3) ligand field. The obtained values of Dq/B are slightly larger than 2.3, which means that the crystal field in the studied crystals is strong. It is worth noting that the obtained values are higher than reported previously for DMANaCr (2.29)[24] and EtANaCr (2.18) and EtANaAlCr

(2.21)[21] and their analogues with K^+ ions, DMAKCr (2.21) and EtAKCr (2.21).[23] These results indicate that the strength of the ligand field is affected by choice of templated organic cation in the metal-formate lattice, e.g. because of the different sizes. The effective radii of DMA^+ and EtA^+ ions are almost the same (272 and 274 pm), however the Am^+ ions are much smaller (146 pm).[47]

This conclusion is in good agreement with the emission spectra of AmNaCr and AmNaAlCr recorded at room temperature under 400 nm excitation (see Fig. 8). Each of them consist of a broad emission band assigned to the spin allowed $^4T_{2g} \rightarrow {}^4A_{2g}$ transition and intense narrow bands which appear due to the $^2E_g \rightarrow {}^4A_{2g}$ spin forbidden transitions. The FWHMs of the broad $^4T_{2g}$ emission is equal to 3303 and 3053 cm^{-1} for AmNaCr and AmNaAlCr, respectively. The maxima of the most intense narrow bands for both samples are located at 697.3 nm (14 335 cm^{-1}). The lower intensity bands centered at 667 (14 993), 677 (14 771), 682.5 (14 652), 689.5 (14 503), 706 (14 164), 726 (13 774) and 753.7 nm (13 268 cm^{-1}) are also present. The intensity of these lines decreases strongly with decreasing temperature, proving their vibronic character. Furthermore, the intensity of the broad emission band decreases with decreasing temperature as well and becomes almost invisible at 77 K for AmNaAlCr. In the case of AmNaCr the spin allowed broad band shifted to *ca.* 802 nm (12 469 cm^{-1}) is still observed at 77 K. The experiment showed that the ^2E_g level lies lower than the $^4T_{2g}$ level and the distance between them is relatively low. The spin allowed $^4T_{2g} \rightarrow {}^4A_{2g}$ transition is observed at higher temperatures together with the $^2E_g \rightarrow {}^4A_{2g}$ due to thermalization of the $^4T_{2g}$ level. By decreasing the temperature to 10 K, the exact positions of Cr^{3+} characteristic lines, R_1 and R_2, could be established. It was found for AmNaAlCr that the vibronic R_1 line is the most intense peak with maximum at 686 nm (14 577 cm^{-1}), while the R_2 line is almost invisible and located 73 cm^{-1} above the R_1 component. The separation between R_1 and R_2 lines is higher than reported for DMANaCr (48.8 cm^{-1}),[24] DMAKCr (45 cm^{-1}), EtAKCr (54 cm^{-1}),[23] and EtANaAlCr (48 cm^{-1})[21] indicating a relatively stronger influence of the crystal field on the energy levels of the chromium ions in AmNaAlCr. For the AmNaAlCr sample some R line sidebands in the range 680 – 707 nm are observed. For the fully concentrated sample, AmNaCr, the intensity of R_1 and R_2 lines sharply drops and become barely visible (Fig. 8). The increase in concentration of Cr^{3+} ions from 5 to 100 % leads to the vanishing of R lines and appearance of intense and sharply structured bands related to the chromium pair lines (Cr–Cr) in the range of 689–696 nm. It can be concluded that the AmNaCr sample exhibits stronger Cr–Cr lines in comparison to previously studied EtAKCr.[23] This effect can be attributed to the smaller ionic size of Na^+ (102 pm) compared with K^+ (139 pm) ions and the smaller size of the templated ammonium ions.

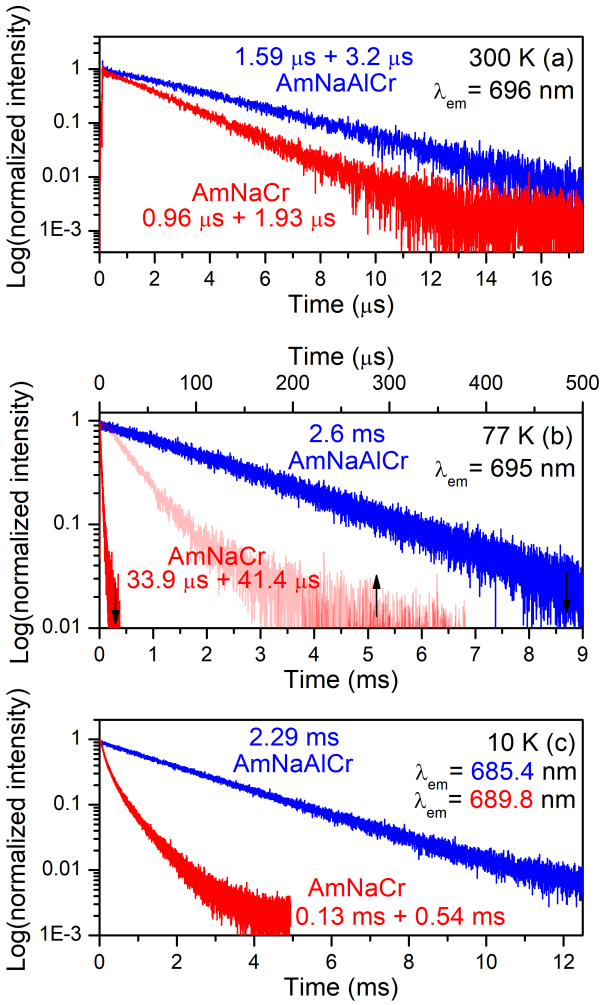

Fig. 9. The luminescence decay profiles of AmNaCr (red) and AmNaAlCr (blue) excited at 400 nm and recorded at (a) 300 K (λ_{em}=696 nm), (b) 77 K (λ_{em}=695 nm) and (c) 10 K (λ_{em}=685.4 and 689.8 nm for AmNaAlCr and AmNaCr, respectively). The bright red plot on figure (b) shows the enlarged profile recorded for AmNaCr, its scale is presented on the top axis.

The low-temperature (at 10 and 77 K) decay curves of the AmNaAlCr sample show exponential decay with a lifetime of 2.29 and 2.6 ms, respectively (Fig. 9). The emission decay time at 300 K is non-exponential due to energy transfer from the ^2E_g energy level to $^4T_{2g}$ state. The strength of this transfer is proportional to the energy separation (ΔE) between ^2E_g and $^4T_{2g}$ levels. The sample that is heavily doped with chromium ions (AmNaCr) shows non-exponential decay at all studied temperatures due to more active non-radiative processes; Cr–Cr energy transfer and Cr–Cr pair energy transfer. The shortest component of emission decay time recorded for the AmNaCr at

10 K is equal to 0.13 ms while the longest one is equal to 0.54 ms. At room temperature the emission lifetimes decrease to 0.96 μs and 1.93 μs, respectively.

4. Conclusions

We have synthesized and investigated heterometallic MOFs crystallizing in the perovskite-type architecture, AmNaCr, AmNaAl and AmNaAlCr. X-ray diffraction data have showed that both compounds adopt trigonal symmetry ($R\overline{3}$ space group) and are isostructural with previously reported AmNaAl. The temperature-dependent Raman studies supported by DSC measurement show that AmNaCr does not undergo any structural phase transitions in the 80–400 K temperature range and its decomposition starts at about 420 K. Our structural DFT data agree well with experimental, and confirm the existence of almost identical HBs in AmNaCr and AmNaAl, with three short HBs and a longer trifurcated HB. Indeed, the hydrogen bonding energy is also calculated to be very similar in the two compounds, and quite strong compared with the Zn^{2+} formate perovskites investigated previously, explaining the absence of a phase transition in both compounds.

Harmonic phonon calculations together with factor group analysis have been used for the assignment of observed IR and Raman bands, especially corresponding to strongly coupled lattice modes. We have performed high-pressure Raman experiments for AmNaCr that showed the onset of two structural instabilities near 0.5 and 1.5 GPa. The first one involves weak distortion of the framework while the second one leads to irreversible amorphization of the sample. DFT simulations under pressure for AmNaCr compound show that the largest relative contraction is along the *c* axis, which leads to a shortening of the tri-furcated HB.

We also show that the emission of Cr^{3+} ions in AmNaCr and AmNaAlCr compounds is characteristic for intermediate ligand field and is slightly stronger in comparison to heterometallic MOFs with the larger ethylammonium and dimethylammonium cations. Furthermore, the optical studies have shown that despite the lack of concentration quenching, the nonradiative processes involving Cr–Cr energy transfer and Cr–Cr pair energy transfer occur in both samples. The obtained emission decay times allow us to conclude that nonradiative transitions play an important role in the investigated samples.

Acknowledgements

This research was supported by the National Science Centre (NCN) in Poland under project No. DEC-2015/17/D/ST5/01339. K. L. S. and A.W. are funded by ERC programme grant no. 277757 and the Royal Society. The authors acknowledge computing support from the UK national supercomputing service (Archer), via membership of the UK Materials Chemistry Consortium which is funded by EPSRC (EP/L000202).

Conflicts of interest

There are no conflicts of interest to declare.

Notes

Electronic Supplementary Information (ESI) available: Figures S1-S4: DSC trace for AmNaCr, calculated and experimental XRD patterns, the temperature evolution of bands corresponding to formate ions; Tables S1-S6: XRD experimental details, geometric parameters for AmNaCr, HBs parameters, factor group analysis and proposed assignment of modes. DFT optimised structures, output from phonon calculations and a gif of the T'(NH_4^+) mode is available from https://doi.org/10.5281/zenodo.1289169.

References

1 A. P. Ramirez, *J. Phys. Condens. Matter*, 1997, **9**, 8171–8199.

2 R. Blinc, *Advanced Ferroelectricity*, Oxford University Press, 2011.

3 F. Hao, C. C. Stoumpos, D. H. Cao, R. P. H. Chang and M. G. Kanatzidis, *Nat. Photonics*, 2014, **8**, 489–494.

4 Y. Yuan, T. Li, Q. Wang, J. Xing, A. Gruverman and J. Huang, *Sci. Adv.*, 2017, **3**, e1602164.

5 A. Stroppa, D. Di Sante, P. Barone, M. Bokdam, G. Kresse, C. Franchini, M.-H. Whangbo and S. Picozzi, *Nat. Commun.*, 2014, **5**, 5900.

6 A. Stroppa, C. Quarti, F. De Angelis and S. Picozzi, *J. Phys. Chem. Lett.*, 2015, **6**, 2223–2231.

7 P. Jain, N. S. Dalal, B. H. Toby, H. W. Kroto and A. K. Cheetham, *J. Am. Chem. Soc.*, 2008, **130**, 10450–

10451.

8 P. Jain, V. Ramachandran, R. J. Clark, H. D. Zhou, B. H. Toby, N. S. Dalal, H. W. Kroto and A. K. Cheetham, *J. Am. Chem. Soc.*, 2009, **131**, 13625–13627.

9 B. Pato-Doldán, M. Sánchez-Andújar, L. C. Gómez-Aguirre, S. Yáñez-Vilar, J. López-Beceiro, C. Gracia-Fernández, A. A. Haghighirad, F. Ritter, S. Castro-García and M. A. Señarís-Rodríguez, *Phys. Chem. Chem. Phys.*, 2012, **14**, 8498.

10 D.-W. Fu, W. Zhang, H.-L. Cai, Y. Zhang, J.-Z. Ge, R.-G. Xiong, S. D. Huang and T. Nakamura, *Angew. Chemie Int. Ed.*, 2011, **50**, 11947–11951.

11 Y. Tian, A. Stroppa, Y. Chai, L. Yan, S. Wang, P. Barone, S. Picozzi and Y. Sun, *Sci. Rep.*, 2015, **4**, 6062.

12 B. Pato-Doldán, L. C. Gómez-Aguirre, J. M. Bermúdez-García, M. Sánchez-Andújar, A. Fondado, J. Mira, S. Castro-García and M. A. Señarís-Rodríguez, *RSC Adv.*, 2013, **3**, 22404.

13 A. Stroppa, P. Jain, P. Barone, M. Marsman, J. M. Perez-Mato, A. K. Cheetham, H. W. Kroto and S. Picozzi, *Angew. Chemie Int. Ed.*, 2011, **50**, 5847–5850.

14 D. Di Sante, A. Stroppa, P. Jain and S. Picozzi, *J. Am. Chem. Soc.*, 2013, **135**, 18126–18130.

15 R. Shang, G.-C. Xu, Z.-M. Wang and S. Gao, Phase Transitions, *Chem. - A Eur. J.*, 2014, **20**, 1146–1158.

16 M. Mączka, A. Gągor, B. Macalik, A. Pikul, M. Ptak and J. Hanuza, *Inorg. Chem.*, 2014, **53**, 457–467.

17 M. Mączka, A. Sieradzki, B. Bondzior, P. Dereń, J. Hanuza and K. Hermanowicz, *J. Mater. Chem. C*, 2015, **3**, 9337–9345.

18 M. Mączka, A. Ciupa, A. Gągor, A. Sieradzki, A. Pikul, B. Macalik and M. Drozd, *Inorg. Chem.*, 2014, **53**, 5260–5268.

19 M. Mączka, A. Pietraszko, L. Macalik, A. Sieradzki, J. Trzmiel and A. Pikul, *Dalt. Trans.*, 2014, **43**, 17075–17084.

20 Y. Yu, R. Shang, S. Chen, B.-W. Wang, Z.-M. Wang and S. Gao, *Chem. - A Eur. J.*, 2017, **23**, 9857–9871.

21 M. Ptak, M. Mączka, A. Gągor, A. Sieradzki, B. Bondzior, P. Dereń and S. Pawlus, *Phys. Chem. Chem. Phys.*, 2016, **18**, 29629–29640.

22 M. Ptak, M. M. Mączka, A. Gągor, A. Sieradzki, A. Stroppa, D. Di Sante, J. M. Perez-Mato and L. Macalik, 2016, **45**, 2574–2583.

23 M. Ptak, A. Gągor, A. Sieradzki, B. Bondzior, P. Dereń, A. Ciupa, M. Trzebiatowska and M. Mączka, *Phys.*

Chem. Chem. Phys., 2017, **19**, 12156–12166.

24 M. Mączka, B. Bondzior, P. Dereń, A. Sieradzki, J. Trzmiel, A. Pietraszko and J. Hanuza, *Dalt. Trans.*, 2015, **44**, 6871–6879.

25 M. Mączka, T. A. da Silva, W. Paraguassu, M. Ptak and K. Hermanowicz, *Inorg. Chem.*, 2014, **53**, 12650–12657.

26 M. Mączka, P. Kadłubański, P. T. C. Freire, B. Macalik, W. Paraguassu, K. Hermanowicz and J. Hanuza, *Inorg. Chem.*, 2014, **53**, 9615–9624.

27 M. Mączka, A. Gągor, N. L. M. Costa, W. Paraguassu, A. Sieradzki and A. Pikul, *J. Mater. Chem. C*, 2016, **4**, 3185–3194.

28 M. Mączka, N. L. Marinho Costa, A. Gągor, W. Paraguassu, A. Sieradzki and J. Hanuza, *Phys. Chem. Chem. Phys.*, 2016, **18**, 13993–14000.

29 A. Ciupa, M. Ptak, M. Mączka, J. G. da Silva Filho and P. T. C. Freire, *J. Raman Spectrosc.*, 2017, **48**, 972–982.

30 Z. Wang, B. Zhang, K. Inoue, H. Fujiwara, T. Otsuka, H. Kobayashi and M. Kurmoo, *Inorg. Chem.*, 2007, **46**, 437–445.

31 Rigaku Oxford Diffraction, 2015, CrysAlisPro Software System, Version 1.171, Rigaku.

32 G. M. Sheldrick, *Acta Crystallogr. Sect. A Found. Crystallogr.*, 2008, **64**, 112–122.

33 G. Kresse and J. Hafner, *Phys. Rev. B*, 1993, **47**, 558–561.

34 J. P. Perdew, A. Ruzsinszky, G. I. Csonka, O. A. Vydrov, G. E. Scuseria, L. A. Constantin, X. Zhou and K. Burke, *Phys. Rev. Lett.*, 2008, **100**, 136406.

35 S. Grimme, J. Antony, S. Ehrlich and H. Krieg, *J. Chem. Phys.*, 2010, **132**, 154104.

36 S. Grimme, S. Ehrlich and L. Goerigk, *J. Comput. Chem.*, 2011, **32**, 1456–1465.

37 A. Togo and I. Tanaka, *Scr. Mater.*, 2015, **108**, 1–5.

38 K. L. Svane, A. C. Forse, C. P. Grey, G. Kieslich, A. K. Cheetham, A. Walsh and K. T. Butler, *J. Phys. Chem. Lett.*, 2017, **8**, 6154–6159.

39 G. Kieslich, S. Sun and A. K. Cheetham, *Chem. Sci.*, 2015, **6**, 3430–3433.

40 M. Maczka, J. Hanuza and A. A. Kaminskii, *J. Raman Spectrosc.*, 2006, **37**, 1257–1264.

41 K. Nakamoto, Wiley InterScience, *Infrared and Raman spectra of inorganic and coordination compounds*,

Wiley-Blackwell, 2008.

42 M. Mączka, K. Szymborska-Małek, A. Ciupa and J. Hanuza, *Vib. Spectrosc.*, 2015, **77**, 17–24.

43 C. H. Wang and R. B. Wright, *J. Chem. Phys.*, 1973, **58**, 1411–1419.

44 R. Samantaray, R. J. Clark, E. S. Choi and N. S. Dalal, *J. Am. Chem. Soc.*, 2012, **134**, 15953–15962.

45 M. Ptak and E. Kucharska, *Vib. Spectrosc.*, 2016, **87**, 40–52.

46 M. Maczka, M. Ptak, K. Hermanowicz, A. Majchrowski, A. Pikul and J. Hanuza, *Phys. Rev. B*, 2011, **83**, 174439.

47 G. Kieslich, S. Kumagai, K. T. Butler, T. Okamura, C. H. Hendon, S. Sun, M. Yamashita, A. Walsh and A. K. Cheetham, *Chem. Commun.*, 2015, **51**, 15538–15541.

48 K. T. Butler, K. Svane, G. Kieslich, A. K. Cheetham and A. Walsh, *Phys. Rev. B*, 2016, **94**, 180103.

49 M. Maczka, A. G. Souza Filho, W. Paraguassu, P. T. C. Freire, J. Mendes Filho and J. Hanuza, *Prog. Mater. Sci.*, 2012, **57**, 1335–1381.